Harnessing Functional Gradients for Enhanced Shock Absorption in Foam Materials

Bhanugoban Maheswaran, Komal Chawla, and Ramathasan Thevamaran *

Department of Mechanical Engineering, University of Wisconsin-Madison, Madison, WI, 53706, USA

June 9, 2026

Abstract

Shock generating high-velocity impacts produce intense, stress waves and rapid accelerations—unlike low-velocity impacts that deform materials under dynamic equilibrium—posing severe risks to human organs, structures, and sensitive equipment. Functionally graded protective foams are promising candidates for shock mitigation due to their spatially tunable density and constitutive profile. However, limited mechanistic understanding of energy absorption and stress attenuation during compaction shock formation in graded foams may hinder their application-specific design. Here, in an integrated experimental and theoretical study, we investigate the compaction shock characteristics of graded foams using intrinsically graded vertically aligned carbon nanotube (VACNT) foams as a model system. Our analysis shows that while energy absorption is governed by compaction shock evolution from impact to the protected boundary, transmitted dynamic stress is primarily dictated by local material impedance. Using our generalizable shock modeling framework applicable to diverse functionally graded foam types, we demonstrate how density and density-dependent constitutive gradation dictate compaction shock characteristics. By selecting appropriate foam types and tailoring functional gradients, simultaneous optimization of energy absorption and transmitted stress attenuation can be achieved, facilitating designs for application-specific shock-mitigation.

Keywords: Functionally graded materials, Dynamic compression, Shock mitigation, Carbon nanotube foams, Shock model

Introduction

Protective material technologies are critical across personal protective equipment (PPE), automotive systems, electronics, and space structures to safeguard against hazardous impacts and crash events. Designing protective materials for shock-generating high-velocity impacts requires more than optimizing bulk properties such as strength, stiffness and energy absorption; it demands a clear understanding of the kinetics and kinematics governing shock propagation [1–3]. Under these conditions, injurious stresses are transmitted through short-duration waves that can damage critical systems or cause severe harm to human organs. Simultaneously,

*Corresponding author: thevamaran@wisc.edu

the protective layer undergoes large, localized deformations and often reaches peak energy-absorption efficiency during the transient wave-propagation phase (Fig. 1(a)). In this regime, inertial effects arising from local density distributions become as important as intrinsic constitutive behavior, jointly governing wave evolution through the material [4]. While conventional design approaches largely focus on stress-equilibrated constitutive responses, overlooking these dynamic effects, in reality, effective shock mitigation design requires deliberate spatial tailoring of both density and local constitutive behavior.

Recently, there has been growing interest in using functionally graded shock-absorbers—particularly graded foams—to achieve superior shock mitigation under blasts and extreme-velocity impacts [5–9]. While most studies demonstrate model accuracy and performance gains, they often stop short of revealing why specific materials and graded profiles work: how the distribution of density and density-dependent constitutive properties govern transmitted stress and energy absorption [10–13]. This gap in mechanistic understanding limits our ability to rationally design graded shock absorbers—to choose both materials and their gradients—to mitigate high velocity impacts. Moreover, much of the prior work on graded foams has remained largely theoretical owing to limitations in experimentally investigating truly continuously graded materials—due to their lack of practical fabrication routes. The fabrication of continuously graded structures has only recently become feasible with advances in additive manufacturing and 3D printing technologies, which enable spatial control over density and structure [7, 8, 14–16]. Even so, producing smoothly varying, precisely tailorable gradients remains challenging, as many additive manufacturing approaches still struggle with fine, continuous transitions in material distribution [17–20].

In this context, intrinsically graded nanofibrous vertically aligned carbon nanotube (VACNT) foams offer a distinctive advantage: their synthesis-induced bottom-to-top growth mechanism naturally introduces a smooth functional gradient (Fig.1(e)) which can be tuned through synthesis parameters [21]. VACNT foams exhibit a multi-lengthscale hierarchical network enabling simultaneously high specific-energy absorption, -strength and -modulus under compression while retaining an ultralightweight structure [22–25]. Recent advances in VACNT foams have revealed unique biaxial [26] and thermal transport properties [27] that make them particularly well suited for impact mitigation applications, such as helmet liners. Moreover, their expansive design space—enabled by tunable 2D mesoscale architectures—extends their applicability beyond helmet systems, opening pathways for broader use across diverse impact protection scenarios [28–32]. These distinctive characteristics of VACNT foams, together with their intrinsic functional gradient, makes them not only an ideal model system for probing the dynamic behavior of functionally graded materials but also a promising candidate for next-generation shock-absorbing applications.

In this work, we investigate the dynamic compression response of VACNT foams through a combined experimental-theoretical approach. Experimentally, we employ two complementary impact set-ups: stress-equilibrated Kolsky (split-Hopkinson) bar tests, which probe the constitutive behavior under uniaxial stress,

and shock-inducing direct impact experiments, which capture the formation and propagation of compaction fronts at higher velocities. Guided by these results, we develop a generalizable uniaxial shock modeling framework that explicitly incorporates the functional gradation along the height of the foam.

Our study provides a mechanistic understanding of compaction-shock propagation in functionally graded foams, showing that dynamic stress is governed primarily by local impedance, while energy absorption is controlled by the cumulative response of the material traversed by the advancing front. By tailoring local properties to reduce impedance near the protected end and optimally distributing energy-absorbing capacity along the foam, functionally graded designs can be engineered to simultaneously minimize transmitted stress and maximize energy absorption. Furthermore, by comparing different foam types including commercial polymeric foams and metallic foams, we provide intuitive design considerations, enabling the selection of appropriate foam types and functional gradient designs for application-specific impact conditions.

Functional Gradients in VACNT Foams by Synthesis

We synthesized VACNT foams on silicon substrates coated with a 1 μm thick thermal oxide layer using floating catalyst thermal chemical vapor deposition (tCVD) process. We first placed the substrates inside a 55 mm diameter quartz tube housed within a horizontal tube furnace and maintained at 827 °C temperature and 1 atm pressure and supplied a carrier gas mixture consisting of 95% argon and 5% hydrogen at a total flow rate of 800 sccm. To initiate CNT growth, we injected a feedstock solution of ferrocene (catalyst precursor) dissolved in toluene (carbon source) at a concentration of 0.01 g/ml into the carrier gas using a syringe pump at an injection rate of 0.8 ml/min. CNTs nucleate on the substrate and grow upward as a vertically aligned forest. As the growth occurs, the internal morphology continuously evolves such that the arrangement and packing of CNTs progressively change, leading to a gradual increase in local density along the thickness of the VACNT foam sample. This growth-induced morphological evolution naturally gives rise to a smooth, continuous density gradient through the height of the CNT assembly, which can be tailored by tuning the synthesis parameters [21].

We used synchrotron X-ray scattering and mass attenuation experiments to quantitatively determine the graded local mass density distribution as a function of sample height in our previous study [21]. The density profile, shown in Figure 1(f), reveals a smooth, approximately linear intrinsic density gradient.

The local constitutive properties of VACNT foams—such as the initial buckling stress and effective modulus—are intrinsically linked to the local density and CNT morphology [22]. As a result, the synthesis-induced gradient in density and morphology directly translates into a spatial gradient in constitutive properties along the foam height, essentially giving rise to non-linear continuously stiffening stress-strain response with hysteresis under uniaxial quasistatic compression (Fig.1(g)). The corresponding deformation mechanism

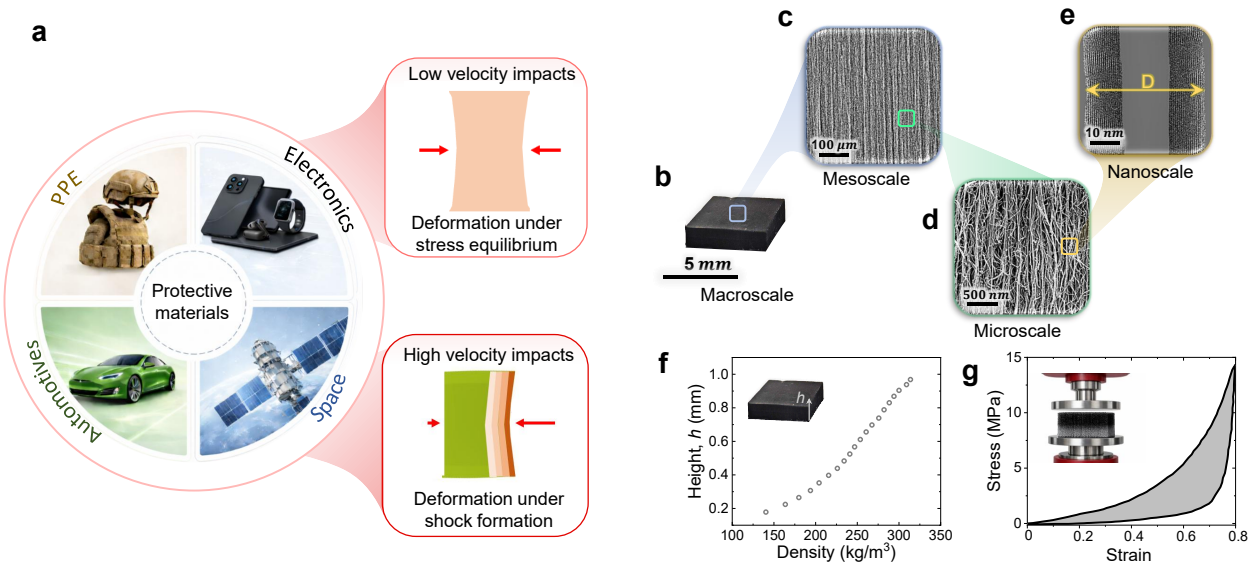

Figure 1: (a) Two high–strain-rate loading regimes governing protective material behavior: stress-equilibrated loading under low-to-moderate velocity impacts, and shock-dominated loading induced by high-velocity impacts and blast events. (b-e) Multi-lengthscale structural hierarchy of VACNT foam: (b) Macroscale free-standing VACNT foam, (c) SEM micrograph of mesoscale VACNT bundles, (d) SEM micrograph of the entangled CNT forest at the microscale, (e) TEM image revealing the multi-walled CNT structure with diameter D , (f) Intrinsic density gradient along the foam height h, quantified using synchrotron X-ray scattering and mass-attenuation measurements [21], (g) Quasistatic uniaxial compression response of a VACNT foam exhibiting non-linear, continuously stiffening loading behavior with hysteretic energy dissipation

is a collective and progressive sequential buckling of nanotubes: deformation initiates in the more compliant, lower-density region and progresses sequentially toward the stiffer, higher-density region [21, 23, 33].

For the experiments conducted in this study, we prepared free-standing VACNT samples with in-plane dimensions of 5 mm × 5 mm and heights ranging from 1 to 2 mm. The bulk density of the samples used in this study varied from 180 to 220 kg/m^3. We used samples from the same batch of CVD synthesis to ensure consistency in sample structure and physical properties as well as dimensions across all quasistatic compression, Kolsky bar, and direct impact experiments conducted in this study. It is worth noting that VACNT foams exhibit mechanical preconditioning under repeated loading–unloading cycles [21]; however, to ensure consistency in our comparisons, all compression responses were evaluated using unpreconditioned pristine samples. We performed at least 3 tests for each experiment and present the average response as the representative responses.

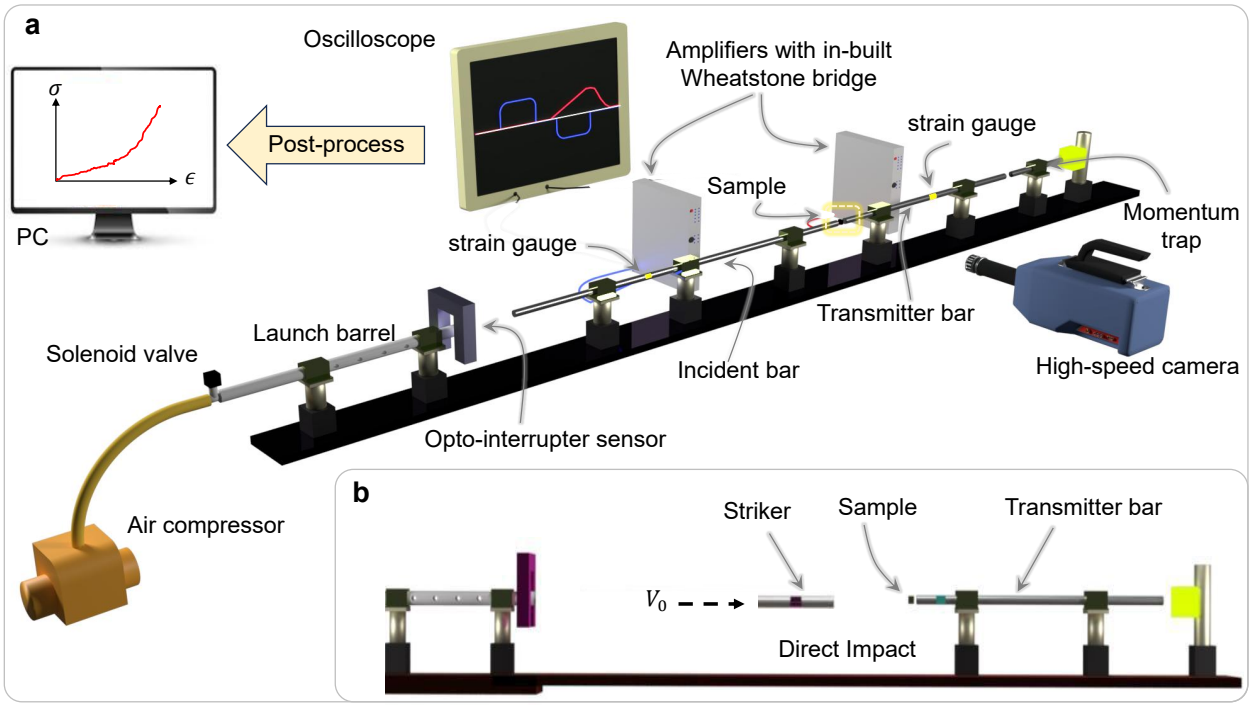

Figure 2: (a) Illustration of the tabletop Kolsky bar experimental setup, including the striker launching system, incident and transmitter bars, strain-gauge–based data acquisition hardware, and synchronized in situ high-speed imaging for dynamic deformation visualization, (b) Illustration of the direct-impact experimental setup with the incident bar removed, in which the sample is impinged directly onto the fixed transmitter bar to facilitate shock-inducing impacts (similar synchronized in situ high-speed imaging was employed).

Dynamic Compression Experiments

Kolsky bar-experiments

The Kolsky bar technique enables dynamic characterization of materials over a wide range of high strain rates while ensuring uniaxial stress equilibrium under nominally constant strain rate loading. We first characterized the high strain rate compression response of VACNT foams under various strain rates using a custom-designed, table-top Kolsky bar experiment. Our experimental setup consists of incident, transmitter, and striker bars, a compressed gas-driven striker launcher, a momentum-trapping mechanism, strain gauges, high-speed data acquisition hardware with appropriate signal conditioning and a high-speed camera for in-situ imaging. Both the incident and transmitter bars were made of aluminum (density 2700 kg/m^3 and modulus 72.2 GPa) and had a diameter of 9.5 mm, with lengths of 900 mm and 700 mm, respectively. The striker bars were slightly larger in diameter (12 mm) to ensure planar impact on the incident bar and their lengths varied from 120-180 mm. We achieved different dynamic strain-rates by varying the impact velocities of the striker bars.

We used resistive strain gauges (Micromeasurements CEA-13-250UNA-350) to measure the incident and reflected pulse signals in the incident bar and used semiconductor strain gauges (Kyowa KSPB-1-350-E4) to

measure the weak transmitted pulse signals in the transmitter bar. Both the strain gauges were connected in a Wheatstone half-bridge configuration using a signal conditioning amplifier (Vishay-Inter technology 2310). We used a 1 GHz oscilloscope (Tektronix MDO34) to trigger, collect, and visualize the raw signals obtained during the dynamic loading of the sample. We later used a customized MATLAB script to post-process the acquired signals to obtain the test data.

We used a high-speed camera (Photron Fastcam SA-Z with a Nikon macro (magnification 1:1) lens) to visualize the deformation mechanisms during the dynamic loading process. The high-speed camera captured the images at a resolution of 256×128 pixels with a frame rate of 300 000 fps. To enhance the visibility of VACNT foams—originally black in color—by ensuring adequate light reflection during the deformation, we coated the sample surface with a coarse speckle of white paint. The comprehensive schematic illustration of our Kolsky bar set-up is given in Figure 2(a).

Direct-impact experiments

To achieve shock-inducing impact conditions, we modified the Kolsky bar set-up into a direct-impact experimental setup (Fig.2(b)). Here, the sample was placed against the fixed aluminum transmitter bar and impacted by launching strikers with strain gauges attached near their impact end at significantly higher velocities ranging from 10-20 m/s. The aluminum strikers used for this direct-impact experiments had a diameter of 9.5 mm (matching the transmitter bar) and a length of 150 mm. To directly measure the impact velocities, we employed a photo interrupter (PASCO wireless smart gate) at the exit of the barrel of striker launcher. We used the similar high speed imaging protocol that we used for Kolsky bar experiments to visualize the in-situ deformation mechanisms during the direct-impact. In both Kolsky bar and direct impact experiments, we investigate two different scenarios determined by the orientation of the density gradient within the sample relative to the ends of the impact and transmitter bar. When the low-density end of the sample aligns with the impact end, we designate this configuration as positive gradient impact (PGI). Conversely, when the high-density end of the sample is positioned near the impact, we refer to this arrangement as negative gradient impact (NGI).

Results and Discussion

Experimental Results

We characterized the constitutive response of VACNT foams under stress-equilibrated dynamic compression over a range of high strain rates, including 3400 s^{-1}, 4700 s^{-1}, and 7400 s^{-1}. Across all dynamic tests, satisfactory stress equilibrium (Fig.3(c)) and nominally constant strain-rate loading were achieved (Fig. 3(b)) [34]. Remarkably, the compressive constitutive responses were strain-rate independent across quasistatic

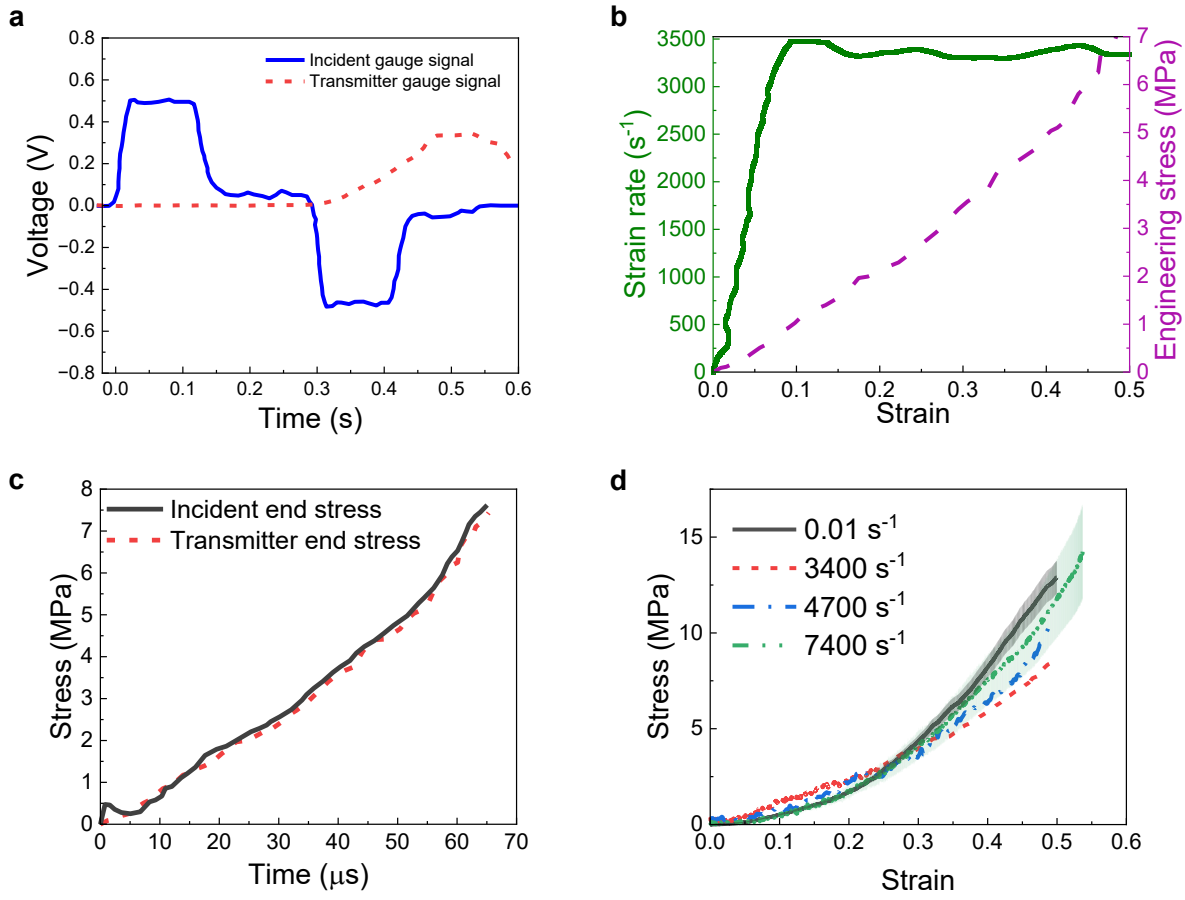

Figure 3: (a) Representative raw waveforms recorded during a Kolsky bar experiment, showing signals from the incident-bar strain gauge and the transmitter-bar strain gauge, (b) Evolution of sample strain-rate and stress with strain demonstrating near–constant strain-rate loading throughout the test, (c) Comparison of the net stress at the left incident bar interface end (calculated from incident + reflected signals) with the right transmitter bar interface end of the sample (calculated from transmitted signal), confirming the attainment of dynamic stress equilibrium, (d) Compressive constitutive response of VACNT foams measured under quasistatic and high-strain-rate loading, highlighting the strain-rate–independent behavior (representative standard deviations in the measurements are shown for the lowest and highest strain rate experiments).

to dynamic strain rates (Fig.3(d)). Even when compared to the quasistatic uniaxial compression response measured at a strain rate of 0.01 s^{-1} (using an Instron ElectroPuls E3000), the high-strain-rate responses closely follow the same curve. As shown in our recent work, the rapid stick-slip van der Waals interactions between nanotubes, which occur on timescales far shorter than the externally imposed loading, manifests as rate-independent macroscopic response [35]. The present results further support this mechanism by experimentally confirming strain-rate-independent constitutive response spanning quasistatic to highly dynamic strain-rate regimes.

Recognizing the presence of an intrinsic functional gradient along the height of the VACNT foams, we conducted the Kolsky bar compression tests in both PGI and NGI orientations. The measured constitutive responses in the two orientations were essentially unchanged, indicating that the stress-equilibrated response

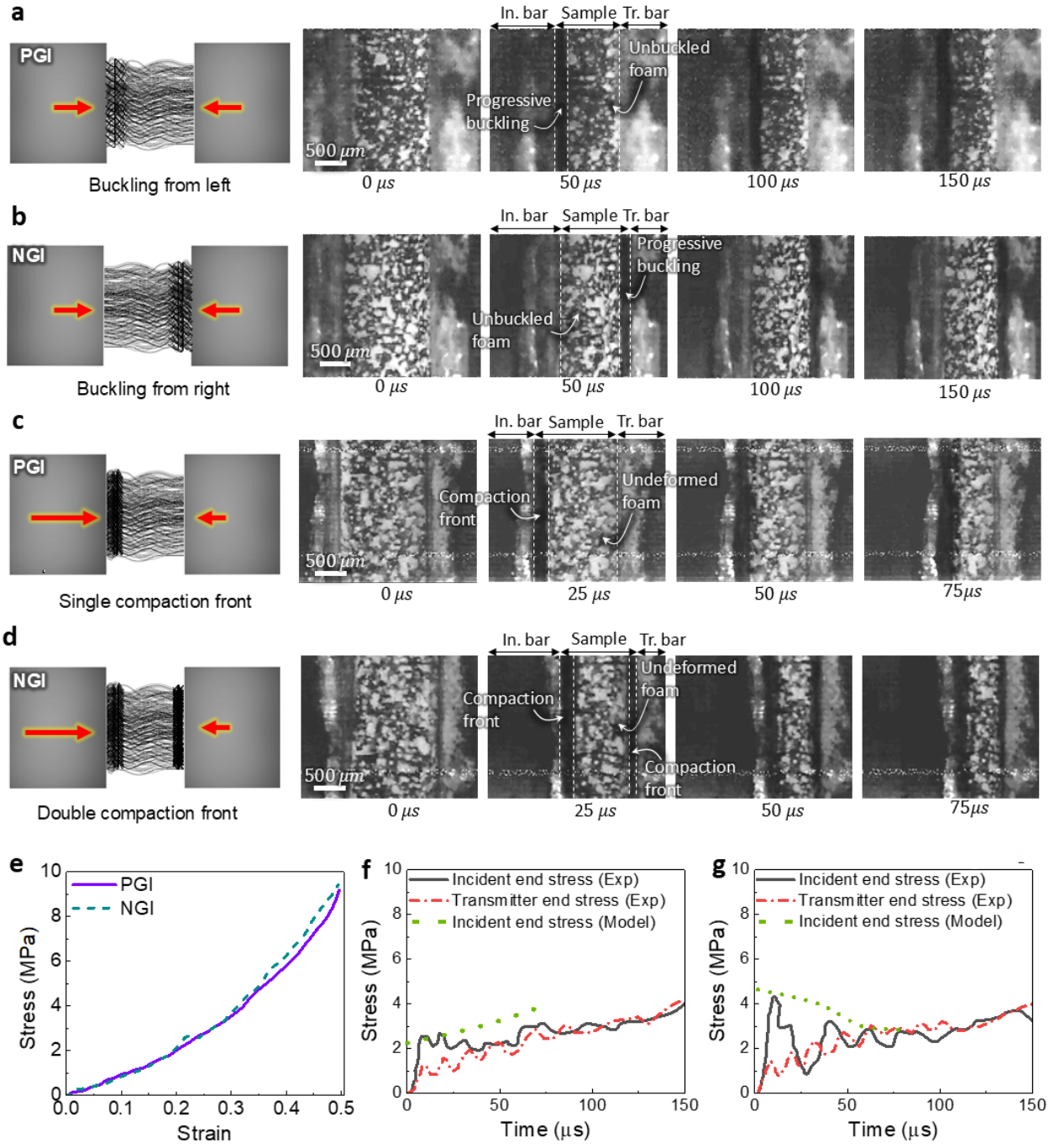

Figure 4: In-situ high speed images of the deformation mechanisms: Collective progressive buckling initiating from the (a) low-density-impact end for the positive gradient impact (PGI) and (b) from the low-density-distal end for the negative gradient impact (NGI) under stress-equilibrated Kolsky bar compression, (c) formation of a single compaction front at the low-density-impact end for PGI and (d) formation of compaction fronts at both the high-density-impact end and the low-density-distal end for NGI under shock-inducing direct impacts, (e) constitutive responses measured from Kolsky-bar experiments for PGI and NGI orientations; (f-g) evolution of stress calculated from incident- and transmitted-bar strain-gauge signals with incident end stresses calculated from analytical model for the (f) PGI and (g) NGI orientations.

was insensitive to impact orientation (Fig.4(e)). This observation further confirms that the dynamic stress equilibrium was not affected by the direction of loading relative to the functional gradient at these strain rates. High-speed in situ imaging further revealed that, under stress-equilibrated dynamic compression, a sequentially progressive collective buckling of CNTs occurs beginning at the low-density region, similar to that observed in quasistatic uniaxial compression (Fig.4(a-b)). Importantly, this deformation mechanism was consistent across all tested dynamic strain rates and was independent of impact orientation, further confirming that the underlying deformation mechanism remains unchanged and microstructurally controlled under stress-equilibrated uniaxial compression, irrespective of the strain rate.

In contrast to these Kolsky bar experiments, the deformation response was highly sensitive to the impact orientations in direct-impact experiments, where the dynamic stress equilibrium was not achieved over the initial phase of loading, even at large deformation levels (Fig.4(f,g)). For PGI, a sharp, discontinuous, compaction front formed at the low-density impact end and rapidly propagated through the sample toward the higher-density regions (Fig.4(c)). For NGI, a similar compaction front initiated at the high-density impact end; however, almost immediately following impact, a second weaker compaction front emerged at the distal, low-density end (Fig.4(d)). Similar orientation-dependent evolution of deformation patterns similar to those observed here has been reported in several prior studies including foam specimens with varying area and [36] graded honeycomb structures [15]. Such emergence of dual compaction zones under NGI has been attributed to the development of highly localized stresses at both ends of the sample: upon impact, a high-intensity stress wave is generated that is sufficient to induce crushing in the high-density region near to the impact interface; simultaneously, a rapidly propagating elastic wave travels through the sample, reaches the distal fixed low-density end, and reflects back with amplified magnitude sufficient to crush the low-density region, ultimately resulting in the near-simultaneous formation of compaction zones at both ends of the foam [37].

From direct impact experiments it was clear that, shock-inducing impacts drive the material away from stress equilibrium, resulting in pronounced spatial stress inhomogeneity, where the deformation behavior and the corresponding stress response (Fig.4(f,g)) becomes highly sensitive to the underlying functional gradient within the protective layer. In the following sections, we provide insights into this functional gradient-governed compaction shock behavior using an analytical shock modeling framework.

Analytical Shock Model

Several studies have developed analytical [11, 36, 37] and finite-element [36, 38, 39] frameworks to study compaction-wave propagation in graded foam materials, predicting single fronts under PGI and dual fronts under NGI. However, most of these models assume rigid–perfectly plastic–locking (R-P-P-L) response that overlook the continuously evolving response of soft materials, limiting applicability to realistic foams materials that undergo gradual densification. Karagiozova et al. [11] addressed this by incorporating realistic stress-

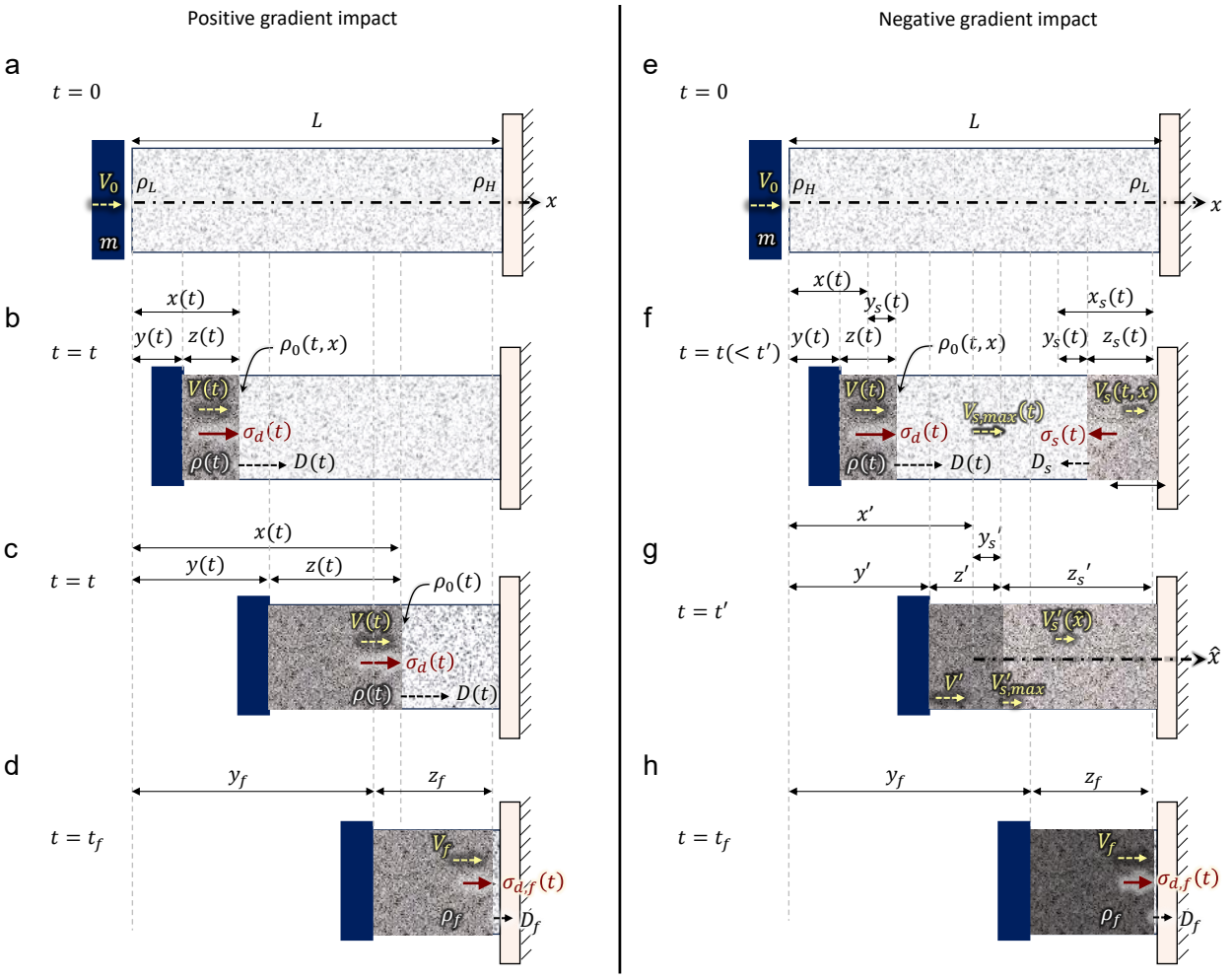

Figure 5: Illustrations of compaction-front evolution with the associated time-dependent state variables. (a) Positive gradient impact (PGI) at $t = t_0$. (b) A single compaction front propagates from the low-density impact end at $t > 0$, with (c) showing continued front advancement without a change in the governing mechanics. (d) The impact-end compaction front reaches the distal end at $t = t_f$. (e) Negative-gradient impact (NGI) at $t = t_0$. (f) Dual compaction fronts propagate from the high-density impact end and the low-density distal end for $t_0 < t < t'$, prior to intersection. (g) Post-intersection evolution of the impact-end compaction front for $t \geq t'$. (h) The impact-end compaction front reaches the distal end at $t = t_f$.

strain responses of the foams, and capturing compaction strains based on particle velocity and dynamic stress. Here, we extend this model to a non-dimensional generalized framework, capturing orientation-dependent compaction fronts in functionally graded foams while clarifying the governing wave mechanics. Throughout this framework, we consider a one-dimensional, linearly density-graded system of unit cross-sectional area, fixed at one end and impacted by a rigid projectile moving at a constant velocity.

PGI orientation

We consider a one-dimensional wave-propagation problem and model the evolution of a sharp compaction front separating an undeformed region from a compacted, moving region (Fig. 5). At this separating compaction front, the material undergoes jump from an undeformed state to the compacted state. A graded foam of initial length L and constant unit cross sectional area having a linear density gradient $\Theta = (\rho_H - \rho_L)/L$ is impacted at the low-density end (ρ_L) by a rigid projectile (mass per unit area m, velocity V_0) at $t = t_0$, initiating compaction (Fig.5(a,b)). For $t > t_0$, a compacted region and an undeformed region coexist, separated by a front at position $x(t)$ moving with velocity $D(t)$, while the projectile and compacted region move at $V(t)$. The undeformed density ahead of the front is $\rho_0(t, x) = \rho_L + \Theta x(t)$, and the dynamic stress at the front is $\sigma_d(t)$. The stress jump that accelerates material to $V(t)$ is $\sigma_d(t) - \sigma_0(t)$, where $\sigma_0(t)$ is the local plateau stress (or initial buckling stress).

$$\sigma_d(t) - \sigma_0(t) = \rho_0(t)\frac{V(t)^2}{\epsilon(t)}. \tag{1}$$

Let the impact-end displacement be $y(t)$ and the compacted-zone thickness be $z(t)$, such that $x(t) = y(t) + z(t)$. Approximating the moving mass per unit area of the compacted region as the swept-up initial mass, the momentum balance for the combined projectile-compacted region system is given by:

$$\left[m + \rho_L x(t) + \frac{\Theta}{2}x(t)^2\right]\frac{dV(t)}{dt} = -\sigma_d(t). \tag{2}$$

Combining the above relations yields

$$\frac{dV(t)}{dt} = -\frac{\sigma_0(t) + (\rho_L + \Theta x(t))\,\frac{V(t)^2}{\epsilon(t)}}{m + \rho_L x(t) + \frac{\Theta}{2}x(t)^2} \tag{3}$$

The differential equations for evolution of $y(t)$ and the $z(t)$ can be directly written in terms of $V(t)$ and $D(t)$ using following equations,

$$\frac{dy(t)}{dt} = V(t) \tag{4}$$

$$\frac{dx(t)}{dt} = \frac{d(y(t) + z(t))}{dt} = D(t) \tag{5}$$

Using Eqs. 4 and 5, the compaction (engineering) strain in deformed region can be written as,

$$\epsilon(t) = \frac{V(t)}{D(t)} \tag{6}$$

The strain at the compaction front is governed by the uniaxial constitutive stress–strain relation and it can be expressed as a function of velocity through the governing jump conditions (Eq. 36) and constitutive response (Eq. 7) [11]. The model assumes that material traversing the compaction front becomes rigidly attached to the compacted mass and undergoes no further deformation. To capture density-dependent constitutive behavior, we adopt a generalizable power-law stress–strain relation, neglecting strains within the elastic regime, as given below.

$$\sigma(\epsilon, \rho_r(x)) = \sigma_p(\rho_r(x))\Big(1 + \Big(\frac{\epsilon}{\epsilon_d(\rho_r(x))}\Big)^{\lambda(\rho_r(x))}\Big) \tag{7}$$

Here, ρ_r denotes the relative density of the foam with respect to the solid density of the parent material, ρ_s, defined as $\rho_r = \rho_0/\rho_s$. The plateau stress, σ_p, densification strain, ϵ_d, and power-law exponent, λ, are material-specific fitting parameters that scale with the relative density, ρ_r, and generally expressed through power-law relationships [31, 40, 41]: $\sigma_p(\rho_r(x)) = \sigma_{p,0}\rho_r^n$, $\epsilon_d(\rho_r(x)) = \epsilon_{d,0}\rho_r^m$ and $\lambda(\rho_r(x)) = \lambda_0\rho_r^p$.

Finally, to provide a system size-independent general description of compaction-shock behavior, we normalized the governing variables and obtained the non-dimensional governing equations. The normalizations employed are below:

$$\bar{x} = \frac{x}{L},\ \bar{y} = \frac{y}{L},\ \bar{\rho} = \frac{\rho}{\rho_{avg}},\ \bar{\sigma} = \frac{\sigma}{\sigma_{0,avg}},\ \bar{m} = \frac{m}{\rho_{avg}L},\ \bar{V} = \frac{V}{\sqrt{\sigma_{0,avg}/\rho_{avg}}},\ \bar{D} = \frac{D}{\sqrt{\sigma_{0,avg}/\rho_{avg}}},\ \bar{t} = \frac{t}{L/\sqrt{\sigma_{0,avg}/\rho_{avg}}}$$

Here, ρ_{avg} denotes the average density of the graded foam, defined as $\rho_{avg} = (\rho_L + \rho_H)/2$, and $\sigma_{0,avg}$ represents the plateau stress corresponding to ρ_{avg}. Corresponding non-dimensional ODEs can be written as

$$\frac{d\bar{V}(\bar{t})}{d\bar{t}} = -\frac{\bar{\sigma}_0(\bar{t}) + \big(\bar{\rho}_L + \bar{\Theta}\bar{x}(\bar{t})\big)\frac{\bar{V}(\bar{t})^2}{\epsilon(\bar{t})}}{\bar{m} + \bar{\rho}_L\bar{x}(\bar{t}) + \frac{\bar{\Theta}}{2}\bar{x}(\bar{t})^2} \tag{8}$$

$$\frac{d\bar{y}}{d\bar{t}} = \bar{V}(\bar{t}) \tag{9}$$

$$\frac{d\bar{x}(\bar{t})}{d\bar{t}} = \frac{d(\bar{y}(\bar{t}) + \bar{z}(\bar{t}))}{d\bar{t}} = \bar{D}(\bar{t}) \tag{10}$$

For PGI, the non-dimensional density gradient is defined as, $\bar{\Theta} = (\bar{\rho}_H - \bar{\rho}_L) > 0$. Within this framework, the ODEs Eq. 8, 9 and 10 describing the evolution of the compacted region are solved subject to the initial conditions $\bar{V}(0) = \bar{V}_0$ and $\bar{x}(0) = \bar{y}(0) = 0$.

NGI orientation

For the NGI case, the emergence of dual compaction fronts is described using physically motivated simplifying assumptions. Following impact at $t = 0$, two deformation fronts coexist for $0 < t < t'$ (until their intersection at $t = t'$): the primary front initiated at the impact end and a secondary front originating from the distal low-density end (Fig.5(e)). The distal compaction front is triggered by the arrival and reflection of an elastic compressive wave, producing a local stress transient sufficient to initiate deformation through progressive crushing [37]. It is assumed to propagate at an approximately constant effective speed D_s [11]. Within the distal deformed region, a kinematically admissible linear velocity field $V_s(t, x)$ is assumed, varying from zero at the fixed boundary to $V_{s,\max}(t)$ at the moving front, consistent with continuity [11]. The undeformed interior translates with $V_{s,\max}(t)$, while the distal deformed zone grows as the front advances. If the distal compaction front travels a distance with respect to the motion of the interior undeformed region $x_s(t) = D_s t$ and the corresponding deformed thickness is $z_s(t)$, then $y_s(t) = x_s(t) - z_s(t)$, from which the governing kinematics follow.

$$\frac{dx_s(t)}{dt} = \frac{x_s(t)}{t} = D_s \tag{11}$$

$$\frac{dy_s(t)}{dt} = V_{s,max}(t) \tag{12}$$

Under these conditions, the distance advanced by the impact-end compaction front with respect to the motion of the interior undeformed region is given by $x(t) = y(t)+z(t)-y_s(t)$. The material at the compaction front moves with a velocity $V_s(t)$. After applying non-dimensionalization., the governing momentum and kinematic relations can be written as follows:

$$\frac{d\bar{V}(\bar{t})}{d\bar{t}} = -\frac{\bar{\sigma}_0(\bar{t}) + \left(\bar{\rho}_H + \bar{\Theta}\bar{x}(\bar{t})\right)\frac{(\bar{V}(\bar{t})-\bar{V}_s(\bar{t}))^2}{\epsilon(\bar{t})}}{\bar{m} + \bar{\rho}_H\bar{x}(\bar{t}) + \frac{\bar{\Theta}}{2}\bar{x}(\bar{t})^2} \tag{13}$$

$$\frac{d\bar{y}(\bar{t})}{d\bar{t}} = \bar{V}(\bar{t}) \tag{14}$$

$$\frac{d\bar{y}_s(\bar{t})}{d\bar{t}} = \bar{V}_{s,max}(\bar{t}) \tag{15}$$

$$\frac{d\bar{x}(\bar{t})}{d\bar{t}} = \frac{d(\bar{y}(\bar{t}) + \bar{z}(\bar{t}) - \bar{y}_s(\bar{t}))}{d\bar{t}} = \bar{D}(\bar{t}) \tag{16}$$

Here, the non-dimensional density gradient is defined as $\bar{\Theta} = (\bar{\rho}_L - \bar{\rho}_H) < 0$. The governing equation for the propagation of the gradually varying compaction front from the distal end can be derived from a power-balance approach. Specifically, we assume that, at each instant, the rate of change of the total kinetic energy of the system, $\dot{T}$, is balanced by the rate of energy dissipated through material deformation, $\dot{U}$. The total kinetic energy T comprises contributions from the combined projectile mass and deformed region at the impact end, the undeformed interior region, and the deformed region at the distal end, and is defined as follows.

$$T = \frac{1}{2}\Big(m+x(t)\big(\rho_H+\frac{\Theta x(t)}{2}\big)\Big)V(t)^2+\frac{1}{2}\Big(\rho_H(L-(x(t)+x_s(t))+\frac{\Theta}{2}\big((L-x_s(t))^2-x(t)^2\big)V_{s,max}^2+\int_{\xi=0}^{\xi=x_s}\frac{1}{2}(\rho_L-\Theta\xi)V_s(t,\xi)^2 d\xi \tag{17}$$

According to the assumption of linear velocity gradient within the deformed region propagating from the distal end we have, $V_s(\xi,t) = \frac{\xi.V_{s,max}}{x_s(t)}$ for $0 \le \xi \le x_s(t)$. Therefore, Eq. 17 can be rewritten as,

$$T = \frac{1}{2}\Big(m+x(t)\big(\rho_H+\frac{\Theta x(t)}{2}\big)\Big)V(t)^2+\frac{1}{2}\Big(\rho_H(L-(x(t)+x_s(t))+\frac{\Theta}{2}\big((L-x_s(t))^2-x(t)^2\big)V_{s,max}^2+\frac{1}{2}x_s(t)\Big(\frac{\rho_L}{3}-\frac{\Theta}{4}x_s(t)\Big)V_{s,max}^2 \tag{18}$$

Taking the time derivative gives $\dot{T}$:

$$\dot{T} = \left[m + \rho_H x + \frac{\Theta x^2}{2}\right] V\dot{V} + \frac{1}{2}\left[\rho_H + \Theta x\right]\dot{x}V^2 + \left[\rho_H(L-x-x_s) + \frac{\Theta}{2}\left((L-x_s)^2 - x^2\right) + x_s\left(\frac{\rho_L}{3} - \frac{\Theta x_s}{4}\right)\right] V_{s,\max}\dot{V}_{s,\max}$$
$$+ \frac{1}{2}\left[-(\rho_H + \Theta x)\dot{x} + \left(-\rho_H - \Theta(L-x_s) + \frac{\rho_L}{3} - \frac{\Theta x_s}{2}\right)\dot{x}_s\right] V_{s,\max}^2. \tag{19}$$

The total energy used up for material deformation is the sum of absorbed strain energy in the deformed region at the impact end and the energy used to deform the region at the distal end.

$$U(t) = \int_0^{x(t)}\int_0^{\epsilon_i(\zeta,t)} \sigma(\eta,\rho_0(\zeta))\, d\eta\, d\zeta + \int_0^{x_s(t)}\int_0^{\epsilon_s(\xi,t)} \sigma(\eta,\rho_0(\xi))\, d\eta\, d\xi. \tag{20}$$

Taking the time derivative term gives an approximate $\dot{U}$:

$$\dot{U} \approx \frac{1}{2}\sigma_d(x)\left[V(t) - V_{s,\max}(t)\right] + \sigma_s(x_s)V_{s,\max}(t), \tag{21}$$

Now, substituting for $\frac{dV(t)}{dt}$ in the expression: $\dot{T} + \dot{U} = 0$, gives the governing equation for the evolution of compaction front. After non-dimensionalization the governing momentum balance takes the form:

$$\frac{d\bar{V}_{s,max}}{d\bar{t}} = \frac{\bar{\sigma}_d\bar{V} - \frac{1}{2}\left(\bar{\rho}_H + \bar{\Theta}\bar{x}\right)\bar{D}\bar{V}^2 - \frac{1}{2}\bar{B}\bar{V}_{s,max}^2 - \frac{1}{2}\bar{\sigma}_d\left(\bar{V} - \bar{V}_s\right) - \bar{\sigma}_s\bar{V}_{s,max}}{\bar{M}_s\bar{V}_{s,max}}. \tag{22}$$

Where,

$$\bar{\sigma}_d = \bar{\sigma}_0 + \left(\bar{\rho}_H + \bar{\Theta}\bar{x}\right)\frac{\left(\bar{V} - \bar{V}_{s,max}\right)^2}{\epsilon}. \tag{23}$$

$$\bar{D} = \frac{V - V_{s,max}}{\epsilon} \tag{24}$$

$$\bar{M}_s = \bar{\rho}_H\left(1 - \bar{x} - \bar{x}_s\right) + \frac{\bar{\Theta}}{2}\left[(1 - \bar{x}_s)^2 - \bar{x}^2\right] + \bar{x}_s\left(\frac{\bar{\rho}_L}{3} - \frac{\bar{\Theta}}{4}\bar{x}_s\right). \tag{25}$$

$$\bar{B} = -\left(\bar{\rho}_H + \bar{\Theta}\bar{x}\right)\bar{D} + \left[-\bar{\rho}_H - \bar{\Theta}\left(1 - \bar{x}_s\right) + \frac{\bar{\rho}_L}{3} - \frac{\bar{\Theta}}{2}\bar{x}_s\right]\bar{D}_s. \tag{26}$$

-

To describe the evolution of compaction fronts for NGI case, ODEs Eq. 13, 17, 15, 16 and 22 can be solved subject to the initial conditions: $\bar{V}(0) = \bar{V}_0$, $\bar{V}_{s,max}(0) = 0$ and $\bar{y}(0) = \bar{y}_s(0) = \bar{x}(0) = 0$.

As the two compaction fronts propagate inward from opposite ends, they intersect at a finite time, beyond which the kinematics and kinetics become increasingly complex. Although the post-intersection responses for both fronts can be analyzed with additional assumptions, we focus only on the impact-end compaction front, which governs the transmitted stress at the distal end and dominates energy dissipation. Let the fronts intersect at $t = t'$, such that $x(t') = x'$. For $t \geq t'$, a coordinate with respect to the motion of the interior undeformed region $\hat{x} = x - x'$ is introduced, measured from the intersection point toward the distal end, to describe the subsequent evolution of the impact-end front (Fig. 5(g)). Note that, now the advancing impact front propagates into an already deforming region with velocity field $V_s(t, \hat{x})$ over $\hat{x} \in [0,\, z_s']$, given as follows:

$$V_s(t, \hat{x}) = V_{s,max}(t)\big(1 - \delta(t)\big). \tag{27}$$

where, $\delta(t)$ implies the relative further growth in the deformed region from the point of front intersection

$$\delta(t) = \frac{\hat{x}(t)}{z_s'} = \frac{y(t) + z(t) - (y' + z')}{z_s'} \tag{28}$$

For $t \geq t'$, three evolving field variables must be specified within the deforming region ahead of the impact-end compaction front: the density field $\rho_0^+(t', \hat{x})$, the strain field $\epsilon_s^+(t', \hat{x})$, and the corresponding stress field $\sigma_s^+(t', \hat{x})$. These fields characterize the material state immediately prior to further compaction and serve as the state variables at the advancing front for the subsequent evolution. The evolution of the density field within the deformed region ahead of the impact-end compaction front is given by

$$\rho_0^+(t, \hat{x}) = \frac{\rho_0(t', \hat{x})}{1 - \epsilon^+(t, \hat{x})} \tag{29}$$

where, the evolving strain field, $\epsilon_s^+(t', \hat{x})$ can be approximated as,

$$\epsilon_s^+(t, \hat{x}) = \epsilon_s^+(t', \hat{x}) + \frac{V_{s,max}(t) \times (t - t')}{z_s'} \tag{30}$$

The stress-strain relation at the impact-end compaction front is governed by the same uniaxial constitutive law.

$$\sigma_s^+(t, \hat{x}) = \sigma_s^+\left(\epsilon^+(t, \hat{x})\right). \tag{31}$$

With non-dimensionalization, for non-dimensional time $\bar{t} \geq \bar{t}'$, the equations of motion governing the coupled dynamics of the projectile and the impact-end deformed region, may be written as

$$\frac{d\bar{V}(\bar{t})}{d\bar{t}} = -\frac{\bar{\sigma}_s^+\left(\bar{t}, \bar{\hat{x}}\right) + \bar{\rho}_0^+(\bar{t}, \bar{\hat{x}}) \dfrac{\left[\bar{V}(\bar{t}) - \bar{V}'_{s,max}\left(1 - \delta(\bar{t})\right)\right]^2}{\epsilon(\bar{t}) - \epsilon^+(\bar{t}, \bar{\hat{x}})}}{\bar{m} + \left(\bar{\rho}_H + \frac{\Theta}{2}\bar{x}(\bar{t})\right)(\bar{x}(\bar{t}))} \tag{32}$$

$$\frac{d\bar{y}(\bar{t})}{d\bar{t}} = \bar{V}(\bar{t}) \tag{33}$$

$$\frac{d\bar{x}(\bar{t})}{d\bar{t}} = \bar{D}(\bar{t}) \tag{34}$$

Here, the impact end-compaction zone strain is given by,

$$\epsilon(t) = \frac{V(t) - V'_{s,\max}(1 - \delta(t))}{D(t)} = \frac{\bar{V}(\bar{t}) - \bar{V}'_{s,\max}(1 - \delta(\bar{t}))}{\bar{D}(\bar{t})} \tag{35}$$

Solving the governing nondimensionalized ODEs Eq. 32, 33 and 34 subject to the initial conditions $\bar{V}(\bar{t}') = \bar{V}'$, $\bar{y}(\bar{t}') = \bar{y}'$, and $\bar{x}(\bar{t}') = \bar{x}'$ yields the temporal evolution of the impact-end compaction front as it

propagates into the deformed region toward the distal end for $t' \leq t \leq t_f$. Here, $t = t_f$ denotes the arrival time of the impact-end compaction front at the fixed end of the sample.

Model Results and Analysis

We calibrate the model by matching the analytically predicted projectile velocity history, $V(t)$, to experimental measurements for both PGI and NGI cases (Fig. 6(b)). The VACNT foam density gradient is assumed linear with $|\bar{\Theta}| = 0.78$, consistent with high-density foams reported in [21] under similar synthesis conditions (Fig. 1(e)). Prior studies show a linear correlation between local density and constitutive properties such as plateau stress and modulus [24, 42]; accordingly, we take $\sigma_p(\rho_r(x)) = \sigma_{p,0}\rho_r(x)$, $\epsilon_d(\rho_r(x)) = \epsilon_{d,0}\rho_r(x)^m$, and $\lambda(\rho_r(x)) = \lambda_0\rho_r(x)$. Fitting yields $\sigma_{p,0} = 37.25$MPa, $\epsilon_{d,0} = 0.105$, $m = -0.84$ and $\lambda_0 = 3.56$ (Fig. 6(b)). We further assume $\rho_s = 2200\text{kg/m}^3$ and calculate D_s as 400m/s using $\sqrt{E_{avg}/\rho_{avg}}$, where E_{avg} is the modulus calculated from the average of loading and unloading curves up to densification [30, 32]. The calibrated model also captures the experimentally measured impact-end dynamic stress for both PGI and NGI orientations, qualitatively and with decent quantitative agreement (Fig.4(f,g)). Within the normalized model framework, the impact-end dynamic stress is obtained by applying a momentum balance to the decelerating rigid projectile:

$$\bar{\sigma}_{d,pr}(\bar{t}) = -\bar{m}\frac{d\bar{V}(\bar{t})}{d\bar{t}}. \tag{36}$$

To evaluate the effectiveness of functionally graded protective layers, we consider two key metrics: reduction of the dynamic stress at the protected distal end and energy absorption prior to front arrival. Using the calibrated framework, we estimate the normalized final dynamic stress at the distal end $\bar{\sigma}_{d,f}$ (Fig. 6(c)) and the energy-absorption efficiency γ (Fig. 6(d)), defined as the ratio of absorbed energy (Eq. **??**) to the initial kinetic energy $(1/2)mV_0^2$.

Effect of projectile mass and impact velocity on gradient sensitivity to ($\bar{\sigma}_{d,f}$) and (γ)

Here, we clarify how initial conditions—specifically projectile mass and impact velocity—influence the sensitivity of protected-end dynamic stress reduction ($\bar{\sigma}_{d,f}$) and energy absorption efficiency (γ) to the functional gradient. We initially consider two distinct scenarios determined by the projectile mass: (i) a heavy projectile compared to foam mass ($\bar{m} = 5$) (Fig.6(c-d)), (ii) foam mass-matched projectile ($\bar{m} = 1$) (Fig.6(e-f)). For each scenario, we considered 5 different impact velocities: for $\bar{m} = 5$, $\bar{V}_0$ ranges from 1 to 3, while for $\bar{m} = 1$, $\bar{V}_0$ ranges from $\sqrt{5}$ to $3\sqrt{5}$, ensuring equal kinetic energy across two scenarios. Notably, in the higher projectile mass lower impact velocity case, both the $\bar{\sigma}_{d,f}$ and γ are lower than the lower projectile mass and higher impact velocity conditions, despite identical initial kinetic energies (Fig.6(c-f)). It should be noticed

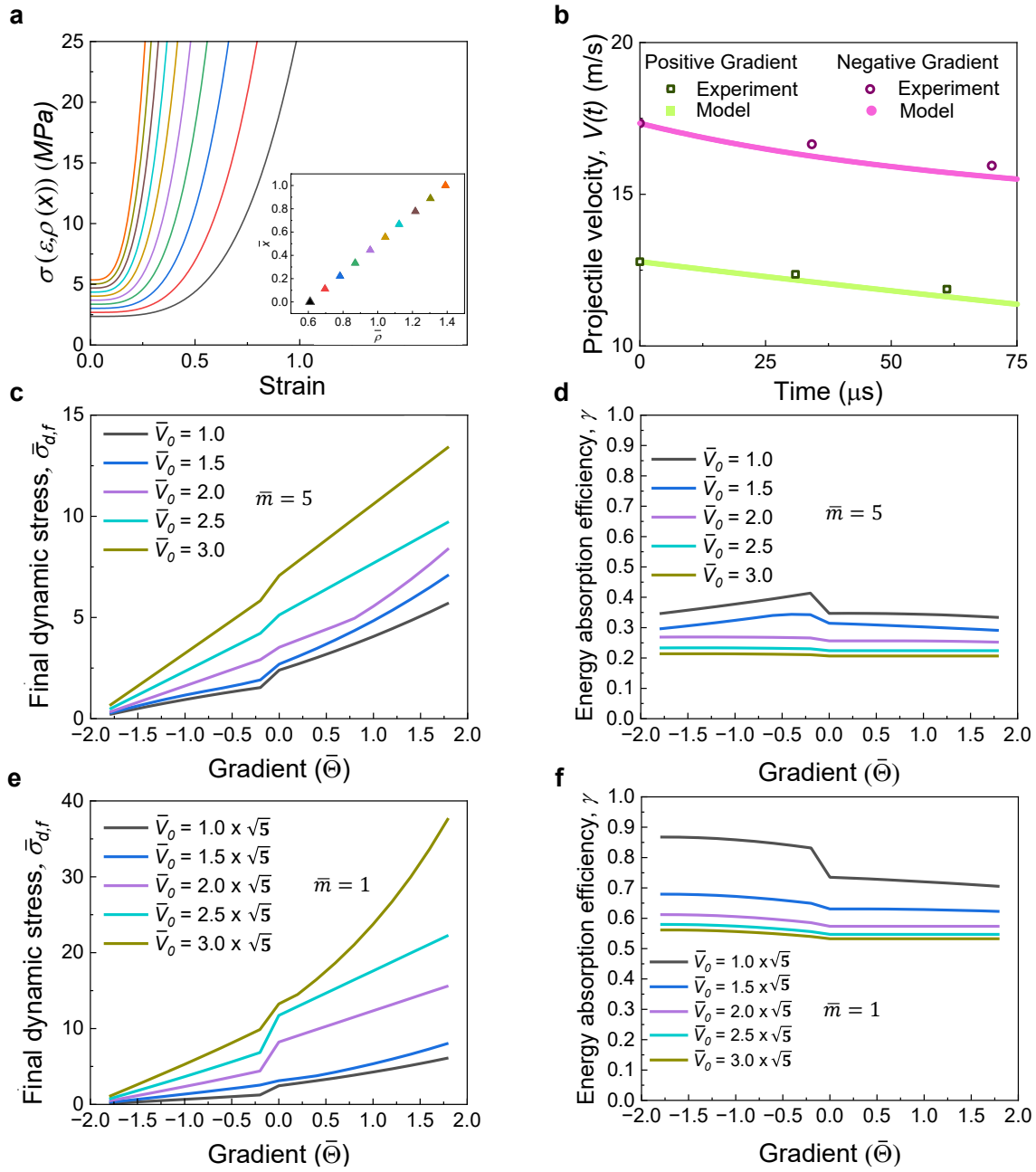

Figure 6: Model calibration and predicted shock-mitigation performance of graded VACNT foams. (a) Density-dependent generalized power-law constitutive responses used for model calibration; inset shows the normalized density profile along the sample length. (b) Comparison of experimentally measured and analytically modeled projectile velocity histories, $V(t)$, after calibration. (c–f) Model-predicted variation of performance metrics with normalized functional gradient for different normalized impact velocities, $\bar{V}_0$, and projectile masses, $\bar{m}$. (c,d) High projectile-mass case, $\bar{m}$=5: (c) final dynamic crushing stress, $\bar{\sigma}_{d,f}$, and (d) energy-absorption efficiency, γ. (e,f) Low projectile-mass case, $\bar{m} = 1$: (e) final dynamic crushing stress, $\bar{\sigma}_{d,f}$, and (f) energy-absorption efficiency, γ

that, while the two scenarios are energetically equivalent, the projectile with lower mass has higher velocity, which has potentially led to higher inertial stresses, thereby higher energy absorption.

However, for both initial conditions $\bar{\sigma}_{d,f}$ systematically reduces as the density gradient shifts from large positive to negative values. (Fig. 6(c,e)). However, depending on the projectile-mass, the influence of functional gradient on γ shows different trends, especially at lower impact velocities. When the projectile mass is higher and the impact velocities are lower (Fig.6(e-f)), we observe that the maximum energy absorption efficiency occurs at mild negative gradients, although dynamic stress at protected end favors steep negative gradients(Fig.6(d)). On the other hand, for low projectile mass scenario, the energy absorption increases as the negative gradients become steeper (Fig.6(f)). Prior studies generally report that negative gradients are more effective in reducing transmitted dynamic stress [10, 11, 43, 44]. However, they present conflicting conclusions regarding energy absorption with some studies favoring positive gradients [10, 44], some favoring negative gradients [11, 43], while the others reporting optimal performance with the ungraded foams [12]. Our analysis shows that negative gradients systematically reduce dynamic stress in general; however, their effect on energy absorption depends on initial conditions, defined by the impact velocity and projectile mass.

Compaction Shock Dynamics in PGI and NGI cases

To intuitively understand how $\bar{\sigma}_{d,f}$ and γ vary between PGI and NGI cases, we examine the evolution of the dynamic stress at the impact compaction front, $\bar{\sigma}_d$, and the rate of normalized energy absorption, $\frac{d\bar{W}}{d\bar{x}}$—normalized by initial kinetic energy—as functions of the compaction front position $\bar{x}$. In this analysis, we consider a linearly functionally graded VACNT foam with $|\bar{\Theta}| = 0.78$ [21], and consider it's PGI and NGI scenarios. Preliminary analysis indicated some trends change progressively as the impact regime transitions from low $\bar{V}_0$ (moderately inertial) to high $\bar{V}_0$ (strongly inertial). Specifically, for PGI, the evolution of $\bar{\sigma}_d$ transitions from a concave-upward to a convex-upward trend as the impact velocity increases from moderately inertial regime to strongly inertial regime for both higher projectile mass and lower projectile mass impact(Fig.7(a) and Fig.8(a)). Accordingly, we focus on the lowest and highest impact velocity, $\bar{V}_0$ considered in each projectile-mass scenario.

The evolution of the dynamic stress at the front directly links the local material state to the global protective performance. This evolution of $\bar{\sigma}_d$ with front position $\bar{x}$ is governed by the orientation of the density gradient with respect to impact. For both projectile mass scenarios, in the PGI case, $\bar{\sigma}_d(\bar{x})$ begins at a lower value at the low-density impact end and increases as the front propagates into the higher-density region (Fig.7(a,d) and Fig.8(a,d)). In contrast, for NGI, $\bar{\sigma}_d(\bar{x})$ starts at a higher value at the high-density impact end and gradually increases as the front advances through the lower-density material. This trend suggests that the dynamic stress at a given front position may be primarily governed by the local constitutive property and inertial properties of the material. The energy absorption rate, $\frac{d\bar{W}}{d\bar{x}}$, follows a similar spatial trend,

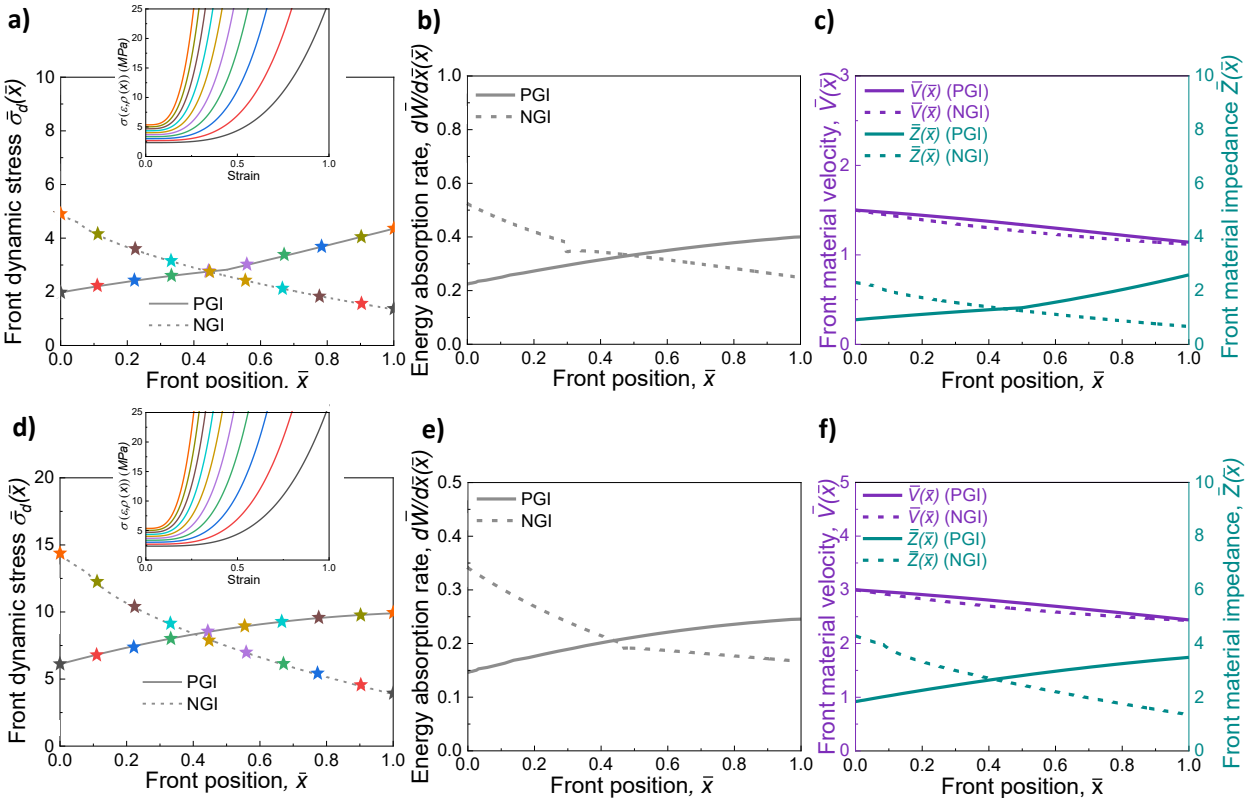

Figure 7: Front evolution analysis for the high projectile mass lower impact velocity scenario for PGI and NGI cases: (a–c) Moderately inertial, low-impact-velocity regime: (a) evolution of normalized dynamic crushing stress, $\bar{\sigma}_d(\bar{x})$, with compaction-front position; (b) corresponding evolution of normalized energy absorption rate with front position $\bar{x}$; (c) evolution of normalized velocity of the combined projectile–deformed region, $\bar{V}(\bar{x})$, and normalized impedance, $\bar{Z}(\bar{x})$, during front propagation. (d–f) Highly inertial, high-impact-velocity regime: (d) evolution of normalized dynamic crushing stress, $\bar{\sigma}_d(\bar{x})$, with compaction-front position; (e) corresponding evolution of normalized energy absorption rate with front position $\bar{x}$; (f) evolution of $\bar{V}(\bar{x})$ and $\bar{Z}(\bar{x})$ during front propagation for both gradient configurations.

indicating that local energy absorption is likewise controlled by the stress sustained at the compaction front (Fig.7(b,e) and Fig.8(b,e)). For NGI, $\frac{d\bar{W}}{d\bar{x}}$ remains consistently higher than in PGI during the early stages, across all impact conditions, allowing NGI configurations to achieve greater energy absorption efficiency, γ. Since γ depends on the cumulative energy absorbed over the entire propagation history rather than on the local response alone, this result implies that the high initial momentum of the projectile more effectively utilizes the energy-absorption capacity of the impact-side material in the NGI case during the early stages of compaction shock propagation.

To inform design for targeted performance, it is essential to identify the material parameters that govern the evolution of stress at the compaction front. Hypothesize that dynamic stress at a given front position, $\bar{\sigma}_d(\bar{x})$, is governed primarily by the local constitutive and inertial properties of the material rather than by the cumulative response of the foam behind the advancing front. The dynamic crushing stress at a front

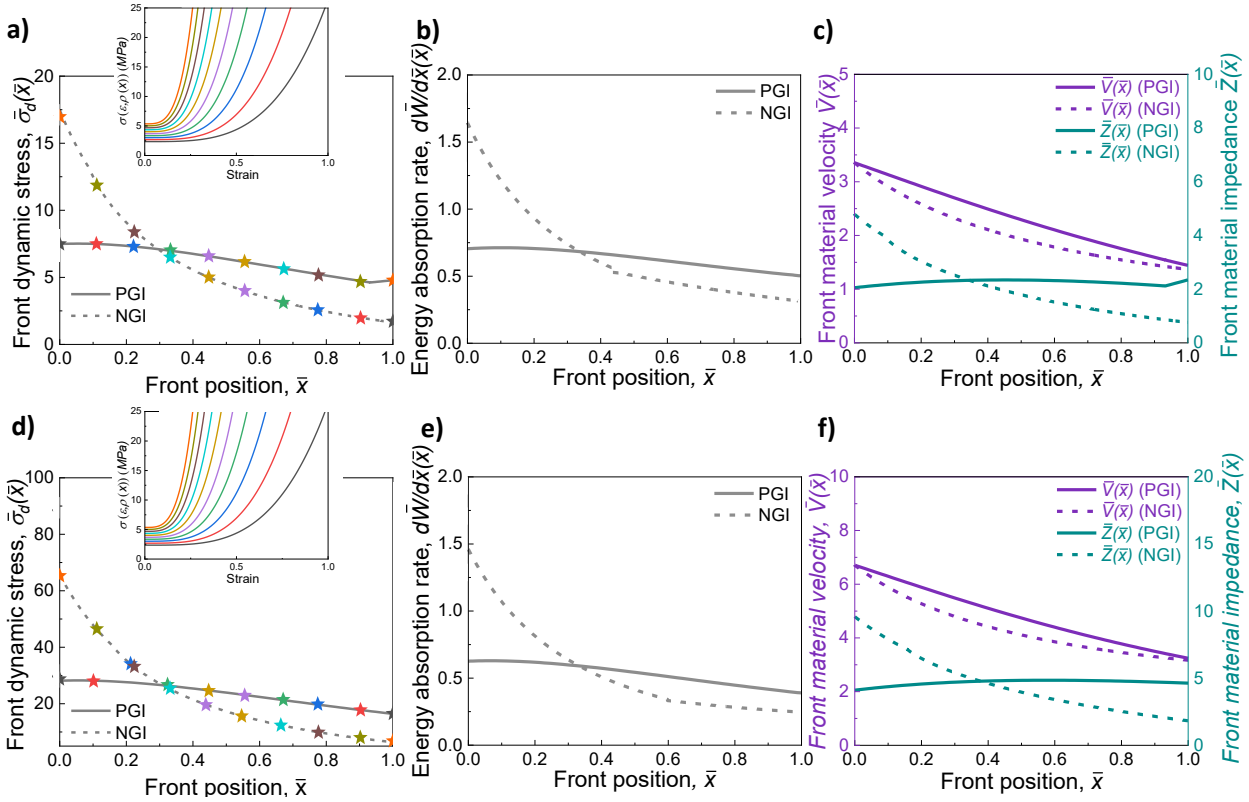

Figure 8: Front evolution analysis for the low projectile mass higher impact velocity scenario for PGI and NGI cases: (a–c) Moderately inertial, low-impact-velocity regime: (a) evolution of normalized dynamic crushing stress, $\bar{\sigma}_d(\bar{x})$, with compaction-front position; (b) corresponding evolution of normalized energy absorption rate with front position $\bar{x}$; (c) evolution of normalized velocity of the combined projectile–deformed region, $\bar{V}(\bar{x})$, and normalized impedance, $\bar{Z}(\bar{x})$, during front propagation. (d–f) Highly inertial, high-impact-velocity regime: (d) evolution of normalized dynamic crushing stress, $\bar{\sigma}_d(\bar{x})$, with compaction-front position; (e) corresponding evolution of normalized energy absorption rate with front position $\bar{x}$; (f) evolution of $\bar{V}(\bar{x})$ and $\bar{Z}(\bar{x})$ during front propagation for both gradient configurations.

position x scales as

$$\sigma_d(x) \sim \sigma_0(x) + \rho_0(x)\frac{V(x)^2}{\epsilon(x)}, \tag{37}$$

where $\sigma_0(x)$ represents the local quasi-static crushing resistance and the second term captures the inertial contribution associated with accelerating material across the front. Within, low-velocity impact regime, the dynamic stress may mainly be governed by the material plateau stress with minor inertial contributions. As the impact velocity increases, the response transitions toward a strongly inertial regime in which the dynamic stress becomes predominantly controlled by the inertial term.

Physically, σ_d reflects the rate of momentum transfer through the material as the compaction front propagates. The momentum transfer occurs through an impulse—force acting over a finite time interval. The timescale governing this momentum transfer, and therefore the magnitude of the stress developed, is controlled by the local mass density and instantaneous constitutive stiffness. Together these quantities define

an effective impedance landscape along the graded foam, which may be expressed as

$$Z(x) = \sqrt{\rho_0(x) E_t(x)}, \tag{38}$$

where $E_t(x) = d\sigma/d\epsilon$ is the tangent modulus evaluated at the stress–strain state selected by the advancing front. Within this framework, the dynamic crushing stress can be interpreted as the sum of a constitutive contribution and an inertial contribution required to accelerate the material,

$$\sigma_d(x) \sim \sigma_0(x) + Z(x)V(x). \tag{39}$$

Consequently, the evolution of inertial dynamic stress is governed by the spatial variation of this impedance landscape together with the particle velocity selected by the front kinematics.

We analyzed the variation of particle velocity, $V(x)$, and effective impedance, $Z(x)$, with the front position, $\bar{x}$, for both projectile-mass scenarios (Fig.7(c,f) and Fig.8(c,f)). In the high-mass case, the evolution of $V(x)$ shows little difference between the PGI and NGI configurations (Fig.7(c,f). In contrast, $Z(x)$ is highly sensitive to the gradient orientation and closely mirrors the observed evolution of the dynamic stress (Fig.7(c,f). For the lower-mass scenario, although $Z(x)$ continues to track the variation in dynamic stress closely, more pronounced differences appear in the evolution of $V(x)$ (Fig.8(c,f). This behavior arises because, when the projectile mass is comparable to the foam mass, the accumulated mass of compacted material becomes significant, causing the velocity evolution to depend more strongly on the local density distribution. Nevertheless, the overall trends support the notion that the dynamic stress is primarily governed by the local inertial and constitutive properties of the material, which can be expressed through the effective impedance. Collectively our analysis suggests, as an optimal design strategy, placing lower-impedance material near the protected end promotes stress attenuation, while concentrating higher energy-absorption capacity near the impact side—by enabling higher initial stresses—enhances overall energy absorption. This design strategy can facilitate simultaneous attenuation of hazardous transmitted stresses while maximizing the absorption of impact-induced kinetic energy in functionally graded systems. However, note that, placing low impedance compliant region near the protected end might also introduce a trade-off between stress attenuation and local densification-induced stress amplification. Excessively compliant regions may undergo rapid local densification during shock propagation, causing a sharp rise in local impedance and potentially generating hazardous stress spikes at the protected boundary. Although such dynamically coupled responses governing graded-foam shock propagation are inherently challenging to predict for deterministic design, the present analytical framework and mechanistic insights provide practical design guidelines for strategically tailoring graded foams to achieve both enhanced energy absorption and improved safety.

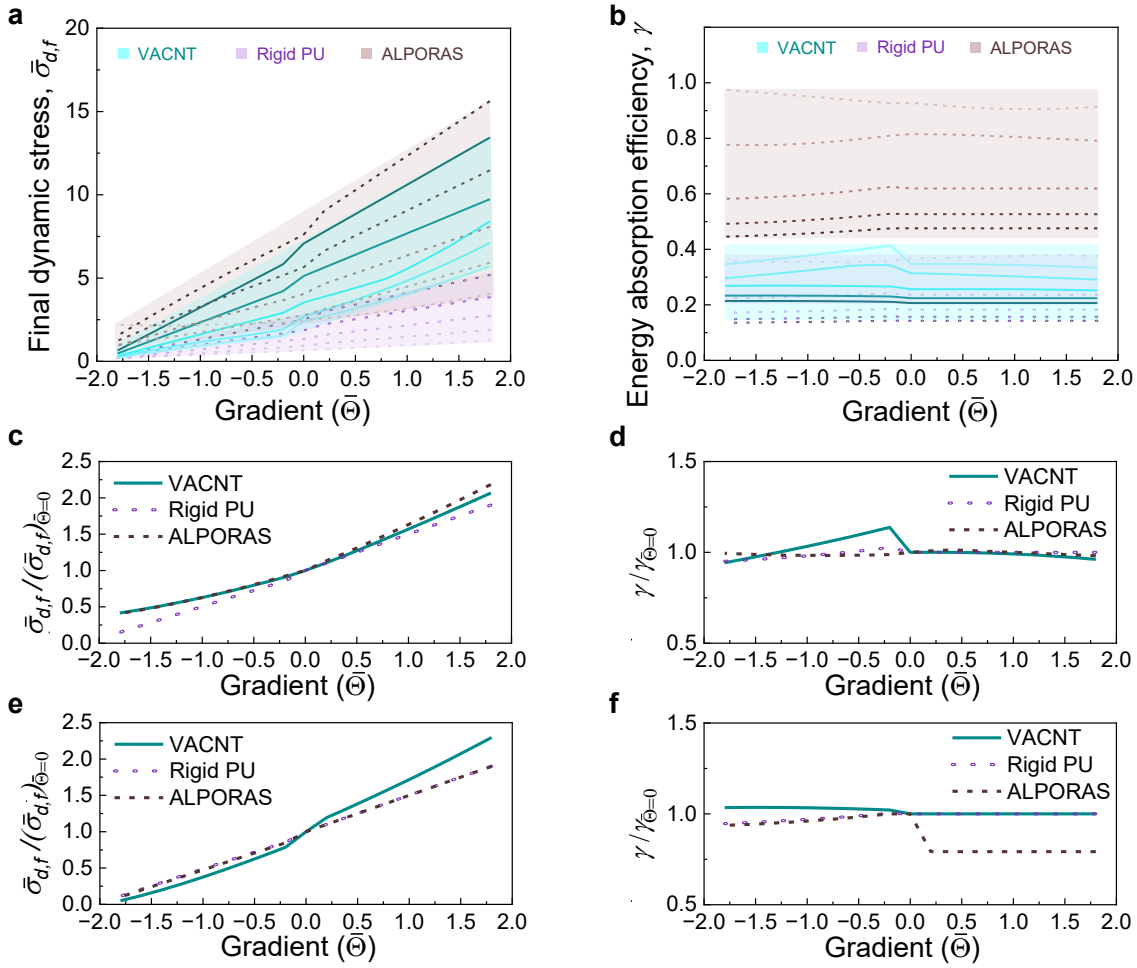

Figure 9: (a–b) Impact-regime maps showing the variation of the performance metrics as a function of functional gradient across foam types with different densities and density-dependent constitutive behavior: (a) normalized final dynamic stress, $\bar{\sigma}_{d,f}$, and (b) energy absorption efficiency, γ, generated for different normalized impact velocities, $\bar{V}_0$. (c–f) Effect of functional grading relative to the corresponding uniform configuration across different foam types: (c–d) moderately inertial, low-velocity regime, showing the ratios of (c) $\bar{\sigma}_{d,f}$ and (d) γ to their respective uniform-case values; (e–f) strongly inertial, high-velocity regime, showing the corresponding ratios of (e) $\bar{\sigma}_{d,f}$ and (f) γ to the uniform-case values.

Compaction Shock Behavior Across Different Foam Types

It is important to understand how the previously discussed compaction-shock dynamics manifest across different classes of functionally gradable foam systems used across different applications. To elucidate the role of gradation in density and density-dependent constitutive behavior in governing dynamic stress and energy absorption across different foam material systems, we extend the framework to typically used functionally graded polymeric and metallic foams. Specifically, we consider the uniaxial compressive responses of rigid polyurethane (PU) foams [45] and ALPORAS aluminum foams [46] over a range of densities. Their constitutive behaviors are represented using the generalizable power-law model (Eq. 7) and incorporated into the compaction-shock framework to analyze the corresponding functionally graded configurations' responses.

The average foam density and constitutive fitting parameters for these foam types are given in Table 1. For consistency, we retain the normalization established for VACNT foams, expressing the performance metrics on a common normalized scale across all foam systems. Meanwhile, the density gradient, $\bar{\Theta}$, is defined relative to the average density (ρ_{avg}) of each specific foam type. This scheme ensures that, although the metrics are directly comparable, the considered functional gradients remain physically representative of each material system, enabling a meaningful comparison of their graded responses and performance. The values of parameters used for the normalization of variables are given in Table 2. For this analysis, we focus only on $\bar{m} = 5$ scenario, where the projectile mass is 5 times the VACNT foam mass.

Table 1: Density and density-dependent constitutive parameters for different foam types

Parameter/(Unit)	VACNT	Rigid PU	ALPORAS
$\rho_{avg}/(kgm^{-3})$	180	112	520
$\sigma_{p,0}/(MPa)$	37.25	39.75	115.60
$\epsilon_{d,0}$	0.105	0.314	0.90
λ_0	3.56	1.027	3.89
n	1	1.57	1.55
m	-0.84	-0.33	-0.28
p	1	-0.83	-0.3

Table 2: Values used for normalization of variables

Parameter	Normalizing value/(Unit)
$\bar{\Theta}$	$\rho_{avg}/(kgm^{-3}/m)$
$\bar{V}$	$123/(m/s)$
$\bar{\sigma}_{d,f}$	$2.74/\ (MPa)$

Figure 9(a,b) show the variation of $\bar{\sigma}_{d,f}$ and γ with functional gradient $\bar{\Theta}$ for functionally graded VACNT, rigid PU, and ALPORAS foams across different impact velocities. All three foam types exhibit similar trends in $\bar{\sigma}_{d,f}$, indicating that negative gradients are generally favorable for reducing transmitted dynamic stress. In contrast, the optimal gradient for maximizing γ depends on the foam type.

Across impact velocities, ALPORAS foams generally produce the highest dynamic stress due to their elevated impedance arising from higher density and stiffness, while rigid PU foams yield the lowest, with VACNT foams exhibiting intermediate behavior (Fig.9(a)). For all foam types, the energy absorption efficiency γ decreases with increasing impact velocity as the material approaches its absorption capacity (Fig.9(b)). Overall, ALPORAS foams exhibit superior energy absorption efficiency, while rigid PU foams, though effective in reducing dynamic stress, are limited by their lower energy absorption capacity. These trends highlight a fundamental trade-off: low-density, low-stiffness foams favor stress reduction but absorb less energy, whereas high-density, stiff foams enhance energy absorption but can transmit higher stresses.

A balanced performance can be achieved using moderately dense and stiff foams combined with tailored functional gradients; however, the optimal choice remains dependent on the specific impact conditions.

We note some interesting gradient-specific effects on dynamic stress and energy absorption across different foam types. For PGI cases in moderately inertial, low-velocity regimes, ALPORAS foams can produce lower dynamic stress than VACNT foams—despite their higher density, stiffness, and plateau stress—owing to their extended plateau regime and delayed densification. However, as the gradient shifts toward negative values, VACNT foams exhibit a more pronounced reduction in dynamic stress across all impact velocities (Fig.9(a)). This indicates that, beyond the imposed linear density variation, the density-dependent scaling of constitutive parameters—such as plateau stress and densification strain—plays a critical role in determining how functional gradients influence performance.

To evaluate the benefits of functionally graded designs relative to their uniform counterparts across different foam systems, we compare the normalized responses of $\bar{\sigma}_{d,f}$ and γ, using values from ungraded configurations as references (Fig. 9(c–f)). Two representative impact velocities are considered: $\bar{V}_0 = 1$ (moderately inertial regime) and $\bar{V}_0 = 3$ (strongly inertial regime). In the low-velocity regime, rigid PU and ALPORAS foams show the pronounced improvement in dynamic stress reduction with negative gradients (Fig.9(c)). However, in terms of energy absorption, both rigid PU and ALPORAS foams exhibit slight improvements, while VACNT foams experience a reduction relative to their uniform counterparts, indicating that gradient-induced benefits are limited under these conditions (Fig.9(d)). In contrast, in the high-velocity regime, VACNT foams demonstrate the most significant gains from negative gradient designs, achieving improvements in both dynamic stress reduction and energy absorption (Fig.9(e-f)). This result highlights that, across different foam types, performance is governed not just by density gradient itself but by how key constitutive parameters scale with density—particularly those relevant to the specific impact regime.

At very low impact velocities, the dynamic stress is strongly influenced by the material's local plateau stress, which governs the resistance to crushing. In this regime, the effect of functional grading is therefore dictated primarily by how the plateau stress scales with relative density. Cellular foams such as rigid PU and ALPORAS typically exhibit a power-law scaling with an exponent of approximately 1.5 [40], whereas VACNT foams follow a near-linear scaling (Table 1). As a result, cellular foams are more sensitive to density gradients under these conditions, leading to more pronounced variations in dynamic stress with gradation. As the impact velocity increases, the response transitions to a strongly inertial regime in which dynamic stress is dominated by wave propagation. In this regime, the local stress is governed by the effective impedance landscape, which depends on both density and the instantaneous tangent modulus. Consequently, constitutive features beyond plateau stress—particularly the density-dependent scaling of densification strain and the post-plateau stiffening exponent—become critical. Foams that exhibit strong density dependence in these parameters can develop sharper spatial variations in impedance, leading to enhanced sensitivity

to functional gradients in both dynamic stress and energy absorption. These observations highlight that gradient performance is not determined by density variation alone, but by the coupled scaling of density and constitutive behavior. Therefore, effective design requires accounting not only for the density gradient but also for the density-dependent scaling of constitutive parameters when selecting foam types and tailoring gradients for specific impact regimes.

Conclusion

We investigated the compaction shock behavior of graded foams using intrinsically graded VACNT foams as a model system. Our experiments probed both stress-equilibrated and shock forming regimes of VACNT foams, employing desktop Kolsky bar experiments for controlled high-strain-rate compression and direct-impact experiments to access compaction shock-formation behavior. The Kolsky-bar experiments revealed a strain-rate-independent uniaxial compression response that closely matches the quasistatic behavior, demonstrating that VACNT foams remain rate independent from quasistatic to dynamic loading regimes. In contrast, the direct-impact experiments revealed a strong dependence of shock formation behavior on the orientation of the functional gradient. Guided by these responses, we develop a generalizable analytical compaction-shock model to capture the orientation-dependent response of functionally graded foams and provide design insights for minimizing hazardous stresses while maximizing energy absorption. Our analysis shows that the transmitted dynamic stress is controlled primarily by the local impedance encountered by the advancing front, whereas energy absorption reflects the cumulative work performed as the front traverses the graded foam. Thus, low-impedance material near the protected end promotes stress mitigation, while higher energy-absorbing capacity near the impact side enhances early-stage kinetic energy absorption, naturally favoring negative functional gradients for simultaneous stress attenuation and enhanced energy absorption. Extending the framework to rigid polyurethane and ALPORAS aluminum foams reveals the physical origins of the trade off between stress attenuation and energy absorption across different foam systems—compliant foams favor stress reduction, whereas denser, stiffer foams enhance energy absorption. Our analysis reveals that this trade-off can be strategically addressed through coupled density-constitutive gradient design, particularly in nanofibrous foams such as VACNTs, where density-dependent post-densification scaling enables tunable impedance evolution and energy absorption.

Declaration of competing interest

The authors declare no conflicts of interest or personal ties that could have influenced the findings in this study

Acknowledgment

We acknowledge the support from the U.S. Office of Naval Research under the PANTHER program award number N00014-24-1-2200 through Dr. Timothy Bentley. We also acknowledge Melissa Schmidt-Landin, Jiyayan Zhang, and Bryan Brady for their assistance with machining components for the experimental instrumentation, and James Engel for valuable discussions regarding high-speed imaging.

Data availability

All data included in the manuscript will be made available upon reasonable request to the corresponding author.

References

[1] Michelle K Nyein, Amanda M Jason, Li Yu, Claudio M Pita, John D Joannopoulos, David F Moore, and Raul A Radovitzky. In silico investigation of intracranial blast mitigation with relevance to military traumatic brain injury. *Proceedings of the National Academy of Sciences*, 107(48):20703–20708, 2010.

[2] Atsuhiro Nakagawa, Geoffrey T Manley, Alisa D Gean, Kiyonobu Ohtani, Rocco Armonda, Akira Tsukamoto, Hiroaki Yamamoto, Kazuyoshi Takayama, and Teiji Tominaga. Mechanisms of primary blast-induced traumatic brain injury: insights from shock-wave research. *Journal of neurotrauma*, 28 (6):1101–1119, 2011.

[3] Marcos Rodríguez-Millán, LB Tan, KM Tse, HP Lee, and MH Miguelez. Effect of full helmet systems on human head responses under blast loading. *Materials & Design*, 117:58–71, 2017.

[4] Tanaz Rahimzadeh, Ellen M Arruda, and MD Thouless. Design of armor for protection against blast and impact. *Journal of the Mechanics and Physics of Solids*, 85:98–111, 2015.

[5] David Hui and Piyush K Dutta. A new concept of shock mitigation by impedance-graded materials. *Composites Part B: Engineering*, 42(8):2181–2184, 2011.

[6] Behrad Koohbor and Addis Kidane. Design optimization of continuously and discretely graded foam materials for efficient energy absorption. *Materials & Design*, 102:151–161, 2016.

[7] Mohammed J Mirzaali, A Herranz De La Nava, Deepthishre Gunashekar, Mahdiyeh Nouri-Goushki, Robin Petrus Elias Veeger, Quentin Grossman, Livia Angeloni, Murali Krishna Ghatkesar, Lidy E Fratila-Apachitei, Davide Ruffoni, et al. Mechanics of bioinspired functionally graded soft-hard composites made by multi-material 3d printing. *Composite Structures*, 237:111867, 2020.

[8] J Cai, KCH Chin, A Gupta, AJ Boydston, and R Thevamaran. Overcoming dynamic stiffness-damping trade-off with structural gradients in 3d printed elastomeric gyroid lattices. *Experimental Mechanics*, 65(6):821–834, 2025.

[9] Mark Smeets, Paul Kauvaka, Kazi Uddin, Behrad Koohbor, and George Youssef. Full-field analyses of density-graded elastomeric foams under quasistatic and impact loadings. *Advanced Engineering Materials*, 25(24):2300994, 2023.

[10] Vijendra Gupta, Addis Kidane, and Michael Sutton. Dynamic characteristics of density-graded cellular materials for impact mitigation. *International Journal of Solids and Structures*, 296:112816, 2024.

[11] D Karagiozova and D Alves. Propagation of compaction waves in cellular materials with continuously varying density. *International Journal of Solids and Structures*, 71:323–337, 2015.

[12] Jie Zheng, Qinghua Qin, and TJ Wang. Impact plastic crushing and design of density-graded cellular materials. *Mechanics of Materials*, 94:66–78, 2016.

[13] Jiagui Liu, Bing Hou, Fangyun Lu, and Han Zhao. A theoretical study of shock front propagation in the density graded cellular rods. *International Journal of Impact Engineering*, 80:133–142, 2015.

[14] Vijendra Gupta and Addis Kidane. Impact response of additively manufactured density-graded open-cell foams. *International Journal of Impact Engineering*, 195:105127, 2025.

[15] Jianjun Zhang, Guoxing Lu, Dong Ruan, and Xiaodong Huang. Experimental observations of the double shock deformation mode in density graded honeycombs. *International Journal of Impact Engineering*, 134:103386, 2019.

[16] Anil Singh, Behrad Koohbor, and George Youssef. Full-field characterizations of additively manufactured composite cellular structures. *Composites Part B: Engineering*, 272:111208, 2024.

[17] Anthony Garland and Georges Fadel. Design and manufacturing functionally gradient material objects with an off the shelf three-dimensional printer: challenges and solutions. *Journal of Mechanical Design*, 137(11):111407, 2015.

[18] S Aadil Hussain, MS Charoo, and Mir Irfan Ul Haq. 3d printing of functionally graded materials: Overcoming challenges and expanding applications. In *Multi-material Additive Manufacturing*, pages 67–97. Elsevier, 2025.

[19] William Oropallo and Les A Piegl. Ten challenges in 3d printing. *Engineering with Computers*, 32(1): 135–148, 2016.

[20] Suhas Alkunte, Ismail Fidan, Vivekanand Naikwadi, Shamil Gudavasov, Mohammad Alshaikh Ali, Mushfig Mahmudov, Seymur Hasanov, and Muralimohan Cheepu. Advancements and challenges in additively manufactured functionally graded materials: A comprehensive review. *Journal of Manufacturing and Materials Processing*, 8(1):23, 2024.

[21] Abhishek Gupta, Claire Griesbach, Jizhe Cai, Steven Weigand, Eric R Meshot, and Ramathasan Thevamaran. Origins of mechanical preconditioning in hierarchical nanofibrous materials. *Extreme Mechanics Letters*, 50:101576, 2022.

[22] Shelby B Hutchens, Alan Needleman, and Julia R Greer. Analysis of uniaxial compression of vertically aligned carbon nanotubes. *Journal of the Mechanics and Physics of Solids*, 59(10):2227–2237, 2011.

[23] Ramathasan Thevamaran, Eric R Meshot, and Chiara Daraio. Shock formation and rate effects in impacted carbon nanotube foams. *Carbon*, 84:390–398, 2015.

[24] Philip D Bradford, Xin Wang, Haibo Zhao, and YT Zhu. Tuning the compressive mechanical properties of carbon nanotube foam. *Carbon*, 49(8):2834–2841, 2011.

[25] Eric R Meshot, Darwin W Zwissler, Ngoc Bui, Tevye R Kuykendall, Cheng Wang, Alexander Hexemer, Kuang Jen J Wu, and Francesco Fornasiero. Quantifying the hierarchical order in self-aligned carbon nanotubes from atomic to micrometer scale. *ACS nano*, 11(6):5405–5416, 2017.

[26] B Maheswaran, K Chawla, and R Thevamaran. Mitigating oblique impacts by unraveling of buckled carbon nanotubes in helmet liners. *Experimental Mechanics*, 64(2):197–209, 2024.

[27] Komal Chawla, Jizhe Cai, Dakotah Thompson, and Ramathasan Thevamaran. Superior thermal transport properties of vertically aligned carbon nanotubes tailored through mesoscale architectures. *Carbon*, 216:118526, 2024. doi: https://www.sciencedirect.com/science/article/pii/S0008622323007716. URL https://www.sciencedirect.com/science/article/pii/S0008622323007716.

[28] Ludovica Lattanzi, Ramathasan Thevamaran, Luigi De Nardo, and Chiara Daraio. Dynamic behavior of vertically aligned carbon nanotube foams with patterned microstructure. *Advanced Engineering Materials*, 17(10):1470–1479, 2015.

[29] Komal Chawla, Abhishek Gupta, Abhijeet S Bhardwaj, and Ramathasan Thevamaran. Superior mechanical properties by exploiting size-effects and multiscale interactions in hierarchically architected foams. *Extreme Mechanics Letters*, 57:101899, 2022.

[30] Komal Chawla, Abhishek Gupta, and Ramathasan Thevamaran. Disrupting density-dependent property scaling in hierarchically architected foams. *ACS nano*, 2023.

[31] Abhishek Gupta, Komal Chawla, Bhanugoban Maheswaran, Daniyar Syrlybayev, and Ramathasan Thevamaran. Embracing nonlinearity and geometry: a dimensional analysis guided design of shock absorbing materials. *Nature Communications*, 16(1):7148, 2025.

[32] Bhanugoban Maheswaran, Komal Chawla, Abhishek Gupta, and Ramathasan Thevamaran. Implicit geometric descriptor-enabled ann framework for a unified structure-property relationship in architected nanofibrous materials. *Extreme Mechanics Letters*, page 102346, 2025.

[33] Shelby B Hutchens, Lee J Hall, and Julia R Greer. In situ mechanical testing reveals periodic buckle nucleation and propagation in carbon nanotube bundles. *Advanced Functional Materials*, 20(14):2338–2346, 2010.

[34] Subramani Sockalingam, Karan Kodagali, Dennis Miller, and Michael A Sutton. On the dynamic equilibrium of square cross-section specimens in compression split hopkinson pressure bar tests. *International Journal of Impact Engineering*, page 105785, 2026.

[35] Abhishek Gupta, Bhanugoban Maheswaran, Nicholas Jaegersberg, Komal Chawla, and Ramathasan Thevamaran. Enduring mechanical memory from the constitutive response of elastically recoverable nanostructured materials. *arXiv preprint arXiv:2509.22678*, 2025.

[36] CJ Shen, Guoxing Lu, and TX Yu. Dynamic behavior of graded honeycombs–a finite element study. *Composite Structures*, 98:282–293, 2013.

[37] CJ Shen, TX Yu, and G Lu. Double shock mode in graded cellular rod under impact. *International Journal of Solids and Structures*, 50(1):217–233, 2013.

[38] Amin Ajdari, Hamid Nayeb-Hashemi, and Ashkan Vaziri. Dynamic crushing and energy absorption of regular, irregular and functionally graded cellular structures. *International Journal of Solids and Structures*, 48(3-4):506–516, 2011.

[39] Jianhui Fan, Jianjun Zhang, Zhihua Wang, Zhiqiang Li, and Longmao Zhao. Dynamic crushing behavior of random and functionally graded metal hollow sphere foams. *Materials Science and Engineering: A*, 561:352–361, 2013.

[40] Lorna J Gibson. Cellular solids. *Mrs Bulletin*, 28(4):270–274, 2003.

[41] GS Langdon, D Karagiozova, MD Theobald, GN Nurick, G Lu, and RP Merrett. Fracture of aluminium foam core sacrificial cladding subjected to air-blast loading. *International journal of impact engineering*, 37(6):638–651, 2010.

[42] Siddhartha Pathak, Nisha Mohan, Elizabeth Decolvenaere, Alan Needleman, Mostafa Bedewy, A John Hart, and Julia R Greer. Local relative density modulates failure and strength in vertically aligned carbon nanotubes. *ACS nano*, 7(10):8593–8604, 2013.

[43] Hu Liu and Bing Feng Ng. Dynamic response of density-graded foam subjected to soft impact. *Composite Structures*, 284:115145, 2022.

[44] Minzu Liang, Zhibin Li, Fangyun Lu, and Xiangyu Li. Theoretical and numerical investigation of blast responses of continuous-density graded cellular materials. *Composite Structures*, 164:170–179, 2017.

[45] Vijendra Gupta and Addis Kidane. Designing density-graded cellular materials for tailored constitutive response. *Composites Part B: Engineering*, 287:111793, 2024.

[46] Ying Cheng, Yanxiang Li, Xiang Chen, Xu Zhou, and Ningzhen Wang. Compressive properties and energy absorption of aluminum foams with a wide range of relative densities. *Journal of Materials Engineering and Performance*, 27(8):4016–4024, 2018.